Nanoscale

ROYAL SOCIETY OF CHEMISTRY

PAPER

View Article Online
View Journal | View Issue

Cite this: *Nanoscale*, 2024, **16**, 9861

A chitosan-coated PCL/nano-hydroxyapatite aerogel integrated with a nanofiber membrane for providing antibacterial activity and guiding bone regeneration†

Xinyuan Deng, ‡[a] Chenghao Yu,‡[b] Xiaopei Zhang,‡[a,b] Xunmeng Tang,[a] Qingxia Guo,[c] Manfei Fu,[b] Yuanfei Wang,*[d] Kuanjun Fang*[a,e] and Tong Wu *[a,b,c]

A guided bone regeneration (GBR) membrane can act as a barrier to prevent the invasion and interference from foreign soft tissues, promoting infiltration and proliferation of osteoblasts in the bone defect area. Herein, a composite scaffold with dual functions of osteogenesis and antibacterial effects was prepared for GBR. A polycaprolactone (PCL)/nano-hydroxyapatite (n-HA) aerogel produced by electrospinning and freeze-drying techniques was fabricated as the loose layer of the scaffold, while a PCL nanofiber membrane was used as the dense layer. Chitosan (CS) solution served as a middle layer to provide mechanical support and antibacterial effects between the two layers. Morphological results showed that the loose layer had a porous structure with n-HA successfully dispersed in the aerogels, while the dense layer possessed a sufficiently dense structure. *In vitro* antibacterial experiments illustrated that the CS solution in the middle layer stabilized the scaffold structure and endowed the scaffold with good antibacterial properties. The cytocompatibility results indicated that both fibroblasts and osteoblasts exhibited superior cell activity on the dense and loose layers, respectively. In particular, the dense layer made of nanofibers could work as a barrier layer to inhibit the infiltration of fibroblasts into the loose layer. *In vitro* osteogenesis analysis suggested that the PCL/n-HA aerogel could enhance the bone induction ability of bone mesenchymal stem cells, which was confirmed by the increased expression of the alkaline phosphatase activity. The loose structure facilitated the infiltration and migration of bone mesenchymal stem cells for better osteogenesis. In summary, such a composite scaffold exhibited excellent osteogenic and antibacterial properties as well as the barrier effect, thus holding promising potential for use as GBR materials.

Received 6th February 2024,
Accepted 23rd April 2024

DOI: 10.1039/d4nr00563e

rsc.li/nanoscale

1. Introduction

Nowadays, treating bone defects such as craniofacial and alveolar bone defects has attracted considerable attention. The guided bone regeneration (GBR) technique has been extensively explored as a significant technique for repairing local bone defects.[1–6] Compared with soft tissues, the regeneration potential of bone is relatively low. In the case of bone defects, adjacent soft tissues severely interfere with bone regeneration due to their fast growth rate. The properties of the GBR membrane allow it to cover the area of the bone defect to form a barrier against foreign soft tissue, thus ensuring normal bone regeneration.[7–9] Generally, an ideal GBR membrane as a bone substitute should have good biocompatibility and biodegradability and a porous structure that allows cell migration and growth. In addition, it is also required to have antibacterial capacity to play antibacterial and bactericidal roles in the area of bone defects and promote healing.[10–13] GBR membranes are commonly categorized into nondegradable and

[a]*Shandong Key Laboratory of Medical and Health Textile Materials, College of Textile & Clothing, Collaborative Innovation Center for Eco-textiles of Shandong Province and the Ministry of Education, Qingdao 266071, China.*
E-mail: kjfang@qdu.edu.cn, twu@qdu.edu.cn
[b]*The Affiliated Hospital of Qingdao University, Qingdao Medical College, Qingdao University, Qingdao 266071, China*
[c]*Institute of Neuroregeneration & Neurorehabilitation, Department of Pathophysiology, School of Basic Medicine, Qingdao University, Qingdao, 266071, China*
[d]*Qingdao Stomatological Hospital Affiliated to Qingdao University, Qingdao, China. E-mail: zhizunbao19@163.com*
[e]*Laboratory for Manufacturing Low Carbon and Functionalized Textiles in the Universities of Shandong Province, Qingdao, State Key Laboratory for Biofibers and Eco-Textiles, Qingdao University, Qingdao 266071, China*

†Electronic supplementary information (ESI) available. See DOI: https://doi.org/10.1039/d4nr00563e

‡These authors contributed equally to this study.

biodegradable membranes. Initially, non-degradable GBR membranes were applied for surgical procedures due to their excellent biocompatibility and mechanical strength. However, the accompanying disadvantage is the need for secondary surgery to remove the GBR membranes, which causes secondary injury to the patient.

With the development of polymers, synthetic or natural polymers such as polylactic acid (PLA), polycaprolactone (PCL), collagen, and chitosan (CS) have been employed to prepare biodegradable GBR membranes.[14] The availability of such biodegradable GBR membranes increased patients' compliance and avoided secondary incisions.[15–19] Among the various synthetic polymers, PCL has been widely used for bone tissue engineering due to its excellent flexibility, mechanical properties, and biocompatibility.[20] CS, a natural polysaccharide, has been widely applied in several fields, such as nerve regeneration, bone repair, and wound healing. Moreover, CS has been reported to exhibit minimal host immune rejection, antibacterial effects against pathogenic bacteria, and good biocompatibility.[21,22] These properties are significant for preventing delayed healing or even non-healing caused by bacterial infection in treating bone defects.[23] In addition, by introducing different organic or inorganic nanoparticles into the material, biological scaffolds can be endowed with specific functions.[24,25] The most promising inorganic material for bone tissue engineering is n-HA, which is the main inorganic phase of bones and has been used in artificial human bones and dental components. Thus, n-HA plays a crucial role in manufacturing new bones due to its non-toxic, bioactive, and osteogenic properties.[26] Although n-HA is a bone repair material that has garnered significant attention, its mechanical properties are insufficient, making it challenging to meet the requirements of clinical bone repair applications. As a type of synthetic polymer with high strength and toughness, PCL can enhance the plasticity of n-HA materials when combined with them. Although PCL has been utilized in bone regeneration scaffolds due to its good mechanical properties, it is noted that its hydrophilicity is poor and the effect of cell adhesion is not ideal. Composite materials containing n-HA, a hydrophilic substance, can enhance the hydrophilicity. As a result, when PCL and n-HA are combined to form composite materials, they complement each other effectively.[27]

Electrospinning is a practical technique for producing nanofibers, which has been employed to prepare nanofiber scaffolds that simulate the natural bone extracellular matrix (ECM). While traditional nanofiber membrane scaffolds are capable of mimicking the ECM of natural tissues, their two-dimensional (2D) structure with small nanofiber pores imposes limitations on cell infiltration.[28–30] Some studies have demonstrated the successful application of nanofiber scaffolds in repairing bone defects. However, their small pore size (1–10 μm) and discrete porous structure hinder the infiltration of bone marrow mesenchymal stem cells (BMSCs) whose size is approximately 25–30 μm, thus hindering the repair performance.[31,32] Therefore, in the field of GBR technology, a three-dimensional (3D) nanostructure scaffold for bone regeneration with continuous and uniformly large pores and excellent mechanical strength demonstrates enhanced ability for bone repair.[33–36] Aerogels are notable owing to their 3D interconnected and adjustable macropore structures.[37–39] Some studies have successfully fabricated 3D nanofiber aerogel scaffolds and demonstrated their ability to enhance bone regeneration and repair.[40–42] Compared with nanofiber membranes, aerogels have larger pores, which can promote the adhesion and migration of bone cells and promote bone repair and regeneration to a greater extent. In addition, research is being conducted on the preparation of guided bone regeneration scaffolds with biofunctions, particularly the antibacterial and osteogenesis capabilities.[43–45] Compared with the GBR material with only a single function, a composite material simultaneously confers antibacterial, barrier, and osteogenic capabilities and can face a more complex bone regeneration environment.

In the present study, we designed a novel biodegradable composite scaffold composed of an aerogel and nanofibers with barrier function, antibacterial ability, and osteogenic performance. The loose layer structure was made of PCL/n-HA aerogel, whose excellent structural properties and large pore size were more conducive to the proliferation and migration of osteoblasts. Random PCL nanofibers were used as the dense layer to serve as a barrier to prevent the infiltration of fibroblasts into the bone defect area. In comparison, BMSCs could proliferate and migrate in the large-aperture aerogel, and the good osteogenic properties of BMSCs in the loose layer were evaluated through *in vitro* osteogenesis experiments. CS solution was used as a middle layer connecting the loose and dense layers while enhancing the antimicrobial effect of the composite scaffold. This work synthesized a multifunctional composite scaffold with barrier function and antibacterial ability for guiding bone regeneration. We also inspire the introduction of natural polysaccharides instead of synthetic polymers as 'glue' to connect loose and dense layers to stabilize the scaffold structure.

2. Materials and methods

2.1. Materials

PCL (average M_n = 80 kDa) and CS were purchased from Sigma-Aldrich Trading Co., Ltd (America). Nano-hydroxyapatite (n-HA; particle size: 60–80 nm), 1,1,1,3,3,3-hexafluoro-2-propanol (HFIP), tertiary butyl alcohol (TBA) and glutaraldehyde (50% in H_2O) were purchased from Shanghai Macklin Biochemical Co., Ltd (China). Gelatin (gel from pig skin) was obtained from Guangzhou Saiguo Biotechnology Co., Ltd (China). Acetic acid (Ac) was obtained from Sinopharm Chemical Reagents (Shanghai) Co., Ltd (China). Fibroblasts (NIH3T3), osteoblasts (MC3T3-E1), and BMSCs were resuscitated from the frozen storage of the ABRM group, Qingdao University. The cell counting kit-8 (CCK-8) was purchased from Shanghai Hongye Biotechnology Co., Ltd (China). The alkaline phosphatase assay (ALP) kit was purchased from Beijing

Pulilai Gene Technology Co., Ltd (China). Artificial saliva, Dulbecco's Modified Eagle's Medium (DMEM), 4,6-diamidino-2-phenylindole stain (DAPI), penicillin–streptomycin, and 4% paraformaldehyde (4% PFA) were bought from Beijing Solarbio Biotechnology Co., Ltd (China). Fetal bovine serum was provided by Gibco (US).

2.2. Preparation of the composite scaffolds

2.2.1 Preparation of PCL/n-HA aligned nanofiber membranes. n-HA powder was added to HFIP to prepare solutions with n-HA concentrations of 5%, 7.5%, and 10%, respectively, and the solution was sonicated for 2 h. Then, PCL was added at a concentration of 10% to obtain the electrospinning solution, stirred for 24 h, and sonicated for 2 h before electrospinning. During the electrospinning process, the PCL/n-HA solution was injected into a 5 mL syringe with a 21-gauge needle, and electrospinning was carried out under the conditions of 11 kV positive voltage, 3 kV negative voltage, 15 cm receiving distance, 1.0 mL h^{-1} injection rate, and 2800 rpm collection. Finally, aligned nanofiber membranes with different concentrations of n-HA were obtained, named M-PCL, M-PHA5, M-PHA7.5, and M-PHA10, respectively.

2.2.2 Preparation of the aerogel (loose layer). The surface of the as-obtained aligned nanofiber membranes was modified for 15 s by plasma treatment using an ion sputter coater (BV10044, China). Then, the aligned nanofiber membranes were cut into short fibers of 25 μm length using a freezing microtome (Leica CM1950, Germany). The short fibers were centrifuged at 2000 rpm for 5 min. Then, TBA solvent was added and centrifuged again. Next, 5% gelatin solution was added to the short fibers and placed in a self-made mold after the mixture. The aerogels were obtained by freeze-drying for 24 h using a freeze dryer (Alpha 1-2LD plus, Germany). The aerogel was crosslinked in glutaraldehyde vapor for 6 h and stored in the dark at a low temperature for further use. Samples with different concentrations of n-HA aerogel scaffolds were named A-PCL, A-PHA5, A-PHA7.5 and A-PHA10, respectively.

To fabricate the composite scaffolds, PCL was dissolved in HFIP (10 w/v%) for electrospinning with a high voltage of 12 kV, a flow rate of 1 mL h^{-1}, and a collecting distance of 15 cm to obtain random PCL nanofibers as the dense layer. 3% (w/v) CS solution was prepared by dissolving the CS powder in 5% (v/v) acetic acid solution. Then, the CS solution was used as 'glue' to connect the loose and dense layers to construct the composite scaffolds. The composite scaffolds containing different concentrations of n-HA were named P/CS-T-PCL, P/CS-T-PHA5, P/CS-T-PHA7.5, and P/CS-T-PHA10, respectively.

2.3. Characterization

The morphology of aligned nanofiber membranes, aerogels, and composite scaffolds was observed using a scanning electron microscope (SEM, Phenom Pure, Holland). The functional groups of the aligned nanofiber membranes, aerogels, and n-HA were characterized by Fourier transform infrared spectroscopy (FTIR, Nicolet is50, US). The crystal structure of n-HA and aerogels was characterized using an X-ray diffractometer (XRD, Bruker D8 Advance, Germany). The surface of aligned nanofiber membranes was modified using a plasma cleaning machine (MiniFlecto, Germany). The machine's working parameters are: power 80 W, frequency 40 kHz, pressure 0.3 mbar, and processing time 15 s. The gas used was oxygen. The wettability of the aligned nanofiber membranes treated with plasma and the untreated aligned nanofiber membranes was measured using a water contact angle testing system (OCA20, DataPhysics, Germany). High magnification SEM images of the different aerogels (A-T-PCL, A-T-PHA5, A-T-PHA7.5, and A-T-PHA10) were used to measure the pore sizes using the Nano measure software. The data were further analyzed and plotted using the Origin software.

The mechanical properties of the aligned nanofiber membranes with different concentrations of n-HA were tested using a universal material testing machine (Instron, US) at room temperature. The membranes (50 mm × 10 mm) were stretched at a rate of 5 mm min^{-1}. The effects of n-HA concentration and aerogel's pore size on the composite scaffolds' compressive mechanical properties were also investigated using a universal material testing machine at room temperature. In this case, the composite scaffolds were fabricated with a diameter of 8 mm and a height of 4 mm, and the tests were repeated at least three times for each group.

In vitro degradation of the composite scaffolds was evaluated in phosphate buffered saline (PBS, PH = 7.4) and artificial saliva, and the artificial saliva was used to simulate the physiological environment. The initial mass (M_0) of the tested composite scaffold was recorded. Then, the scaffold was immersed in a centrifuge tube containing 5 mL of PBS or artificial saliva at 37 °C and 150 rpm. The incubation solution was changed every 2 days. The specimens were collected on days 1, 4, 11, 18, 32, and 46, with 5 parallel samples at each time point. The samples were thoroughly washed with deionized water and freeze-dried to weigh the remaining mass of samples (M_t). The degradation rate at each time point was calculated using eqn (1).

$$\text{Degradation rate}(\%) = \frac{M_0 - M_t}{M_0} \times 100\% \quad (1)$$

2.4. Investigation of cell behaviors

2.4.1. MC3T3-E1 cell proliferation. The aligned nanofiber membranes containing different concentrations of n-HA were precisely cut into appropriate sizes and sterilized under ultraviolet irradiation for 2 h. Briefly, MC3T3-E1 cells were cultured on the different samples at an initial density of 1×10^4 cells per well in a 24-well plate. Cell proliferation was assessed after 1, 3, and 5 days of culture using cell counting kit-8 (CCK-8). Specifically, the culture medium was removed at different time points, and fresh medium with 10% CCK-8 was added to each well. After further incubation for 3 h, the absorbance at 450 nm was measured using a microplate reader.

2.4.2. Cell morphology. The morphology of MC3T3-E1 cells was observed using a fluorescence microscope (Nikon, Japan). The cells were seeded onto aligned nanofibers for 1, 3, and

5 days. After fixation with 4% paraformaldehyde, the cells were washed with PBS, permeabilized with 0.1% Triton X-100, and blocked with 1% BSA in PBS. Subsequently, the cytoskeleton and nucleus were observed with F-actin and DAPI, respectively. Then, the samples were subjected to gradient dehydration with 30%, 50%, 70%, 80%, 95%, and 100% ethanol for 10 min. After air-drying, the samples were imaged by SEM.

2.5. Antibacterial activity evaluation

The antibacterial effect of the composite scaffolds was determined using the absorption method.[46] The broths inoculated with *Staphylococcus aureus* (*S. aureus*, ATCC 25923, a representative Gram-positive bacteria) or *Escherichia coli* (*E. coli*, ATCC 25922, a representative Gram-negative bacteria) were transferred into a constant temperature shaker for 24 h, and the bacterial solution was diluted to 3×10^5 CFU per mL with 0.03 M PBS. 0.03 g composite scaffold with or without CS solution coating was added to a glass bottle and sterilized by ultraviolet irradiation for 30 min. Then, 100 μL of diluted bacterial solution was added. After 18 h, the scaffold was eluted with the addition of 20 mL PBS. Ten-fold gradient dilution solutions were applied to an agar plate with triplet parallel samples and incubated in a 37 °C incubator for 48 h. The samples without the composite scaffolds were used as the control. The antibacterial rate was calculated using eqn (2).

$$E_{\text{anti}}(\%) = \frac{N_c - N_e}{N_c} \times 100\% \quad (2)$$

where E_{anti} represents the antibacterial rate, N_c represents the bacterial number of the control group, and N_e represents the bacterial number of the composite scaffold.

The samples were stained with a live–dead staining kit for 30 min and then washed using PBS three times. The dead bacteria (red fluorescence) and live bacteria (green fluorescence) were observed.

2.6. *In vitro* osteogenesis capability of the composite scaffolds

The osteogenic performance of the composite scaffold was assessed by measuring the ALP activity. BMSCs were seeded on the loose layer of the composite scaffolds (LL-P/CS-T-PCL, LL-P/CS-T-PHA5, LL-P/CS-T-PHA7.5, LL-P/CS-T-PHA10) with different concentrations of n-HA in a 24-well culture plate, with glass slides as the control. After 7 and 14 days of cultivation in an osteogenic medium, a semi-quantitative evaluation of the ALP activity was performed according to the instructions of the ALP detection kit.

2.7. Investigation of the barrier effect of the composite scaffolds

To assess cell infiltration into the composite scaffolds, the BMSCs and NIH3T3 fibroblasts were separately seeded and cultured on the loose and dense layers of the P/CS-T-PHA5 composite scaffold. Briefly, the samples were treated with 75% alcohol vapor for 6 h and ultraviolet radiation for 0.5 h in the ultra-clean platform. After washing with PBS and DMEM three times, the samples were immersed in DMEM supplied with 10% fetal bovine serum and 1% penicillin–streptomycin for 1 h. Subsequently, the BMSCs were incubated on the loose layer of the scaffold at a density of 1×10^5 per well for 7 days. For another investigation, the NIH3T3 fibroblasts were cultured on the dense layer of the scaffold for 7 days. Then, the samples were fixed with 4% paraformaldehyde, embedded in an optimal cutting temperature compound, and subsequently stored overnight at −80 °C. The samples were sectioned into 50 μm slices using a cryostat microtome, and the sections were washed with PBS three times and stained with DAPI for observation.

2.8. Statistical analysis

All experiments were carried out with at least three duplicate samples. The value is presented as mean ± SD. All pairwise comparisons were performed using the Student's *t*-test. $*P < 0.05$, $**P < 0.01$, and $***P < 0.001$ were considered to be statistically significant.

3. Results and discussion

The detailed process of preparing the composite scaffold is shown in Scheme 1. The dense layer was made of a random PCL nanofiber membrane to prevent the filtration of fibroblasts, while the loose layer composed of the PCL/n-HA aerogel was expected to promote the proliferation and migration of BMSCs further. To stabilize the structure and endow the composite scaffold with anti-bacterial properties, the middle layer made of CS solution is integrated into the scaffold. The preparation of the aerogel can be divided into three main steps: electrospinning, frozen section, and freeze-drying.[38,39] The CS solution is applied to the aerogel as the middle layer. By adjusting the applied voltage, flow rate, and the distance between the tip and the CS-coated aerogel, electrospun PCL nanofibers were successfully deposited and the composite scaffolds were constructed.

3.1. Characterization of the composite scaffolds

The morphological characterization of the as-obtained composite scaffold is shown in Fig. 1. Fig. 1a displays the photograph of the composite scaffold consisting of the PCL nanofiber membrane with a smooth surface as the dense layer and the aerogel made of freeze-dried short fibers with a rough surface as the loose layer. We also prepared composite scaffolds with different shapes and sizes, as shown in Fig. S1.† The size and thickness of the composite scaffolds can be controlled. The dimensions of the composite scaffold are shown in Fig. 1b and c. The scaffold had a width of 6 mm and a thickness of 2 mm. Fig. 1d and e indicate that the thickness of the dense layer is around 360 μm. The cross-sectional observation of the composite scaffold is illustrated in Fig. 1f. The existence of the viscous CS in the middle layer helped to stabilize the composite scaffold. The SEM images showed that the loose layer had larger interconnected pores, which exhibited greater porosity

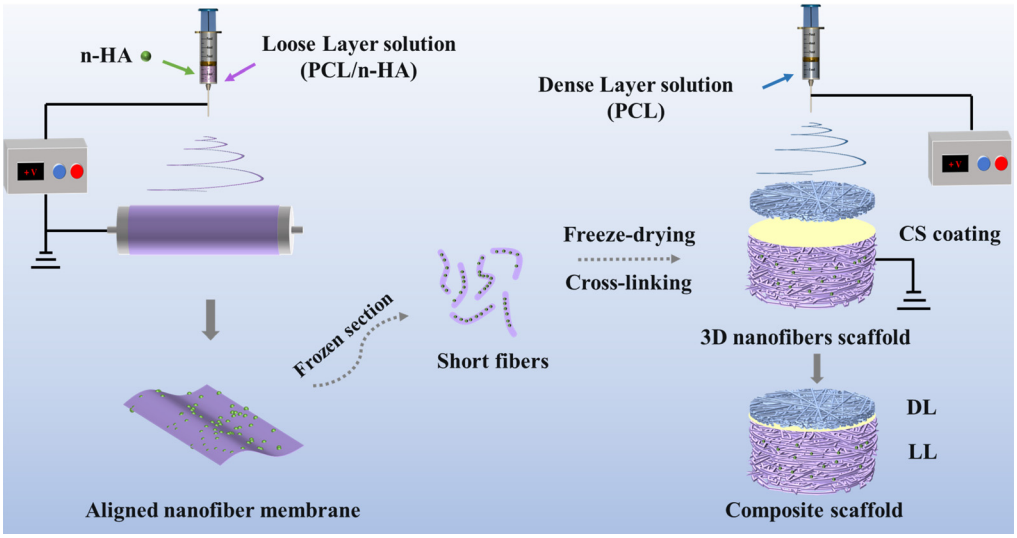

Scheme 1 Schematic diagram of the preparation process of the composite scaffold.

than the dense layer. Fig. S2a† shows the morphology of the PCL nanofiber membrane, illustrating the interlacing of nanofibers in both horizontal and vertical directions, resulting in a dense structure. The diameter of the PCL nanofibers was 782 ± 27 nm (Fig. S2b†).

3.2. Characterization of the aligned nanofiber membranes

3.2.1 Physical characterization. The characterization of the aligned nanofiber membranes is illustrated in Fig. 2. To create fibers with osteogenic properties, various concentrations of n-HA were added to the fibers. n-HA has been reported as an artificially synthesized biodegradable and bioactive material that can promote the growth and regeneration of bone tissues.[26] The fiber morphologies of the aligned nanofiber membranes with different n-HA contents were observed by the SEM images (Fig. 2a). These images confirmed the successful dispersion of n-HA as scattered visible protrusions in the aligned PCL nanofibers. Fig. 2b shows the FTIR spectra of the different aligned fiber membranes and n-HA. For PCL, the band observed at 2942 cm^{-1} was attributed to the asymmetric stretching motion of $-CH_2$, while its symmetric stretching mode was observed at 2865 cm^{-1}. The transmission band at 1721 cm^{-1} indicated the presence of C=O in PCL. Additionally, the distinct band at 1293 cm^{-1} was attributed to the overlap between the C–O and C–C stretching. The bands at 1293 and 1165 cm^{-1} were associated with the asymmetric and symmetric stretching of C–O–C in PCL, respectively. For n-HA, the bands at 559, 601, and 963 cm^{-1} corresponded to PO_4^{3-}, while the bands in the range of 1400 cm^{-1} to 1500 cm^{-1} were attributed to CO_3^{2-}. The FTIR spectra of the composite scaffolds showed both characteristic bands for PCL and n-HA. However, these bands exhibited slight shifts due to the mutual interactions between the components.[26] The water contact angles of M-PCL, M-PHA5, M-PHA7.5, and M-PHA10 aligned nanofiber membranes were all greater than 90° (Fig. 2c). However, the relatively high hydrophilicity of nanofiber membranes is favorable for promoting cell adhesion, proliferation, and migration.[47] In this regard, plasma modification was used on all aligned nanofiber membranes to enhance their hydrophilicity (Fig. S3†).

The addition of n-HA to nanofiber membranes may increase the roughness of fibers, which is beneficial for cell adhesion and migration.[48] A higher content of n-HA can increase osteogenic differentiation. However, the extensive addition of n-HA may lead to a higher risk of aggregation in fibers and poorer mechanical effects.[49,50] The tensile strength of different aligned nanofiber membranes was measured, respectively (Fig. S4†), and the tensile stress–strain curves of aligned nanofiber membranes with varying concentrations of n-HA are shown in Fig. 2d. Fig. 2e–g show the ultimate strain and stress at break and Young's modulus of each scaffold. Table S1† presents the different aligned nanofiber membranes' maximum tensile stress and strain. The tensile stress of M-PCL, M-PHA5, M-PHA7.5, and M-PHA10 membranes was gradually decreased with the increase of n-HA concentration. Even if the two-step ultrasound method is used to disperse n-HA in PCL solution, a higher content of n-HA would contribute to a higher agglomeration risk of n-HA in the fibers and less effective mechanical properties.[49]

3.2.2 The behaviors of MC3T3-E1 cells on the aligned nanofiber membranes. GBR is a surgical procedure that uses a barrier membrane to promote the growth of new bone tissues in bone defect areas due to injury or disease. The barrier membrane is a physical barrier, preventing soft tissue from growing inward. In addition, it allows bone cells to migrate to the bone defect area and form new bone tissues.[9] To meet the clinical requirements, the aerogel made of short nanofibers was employed to provide growth support for osteoblasts and osteogenic differentiation of stem cells. We first evaluated the proliferation of MC3T3-E1 cells on various aligned nanofiber

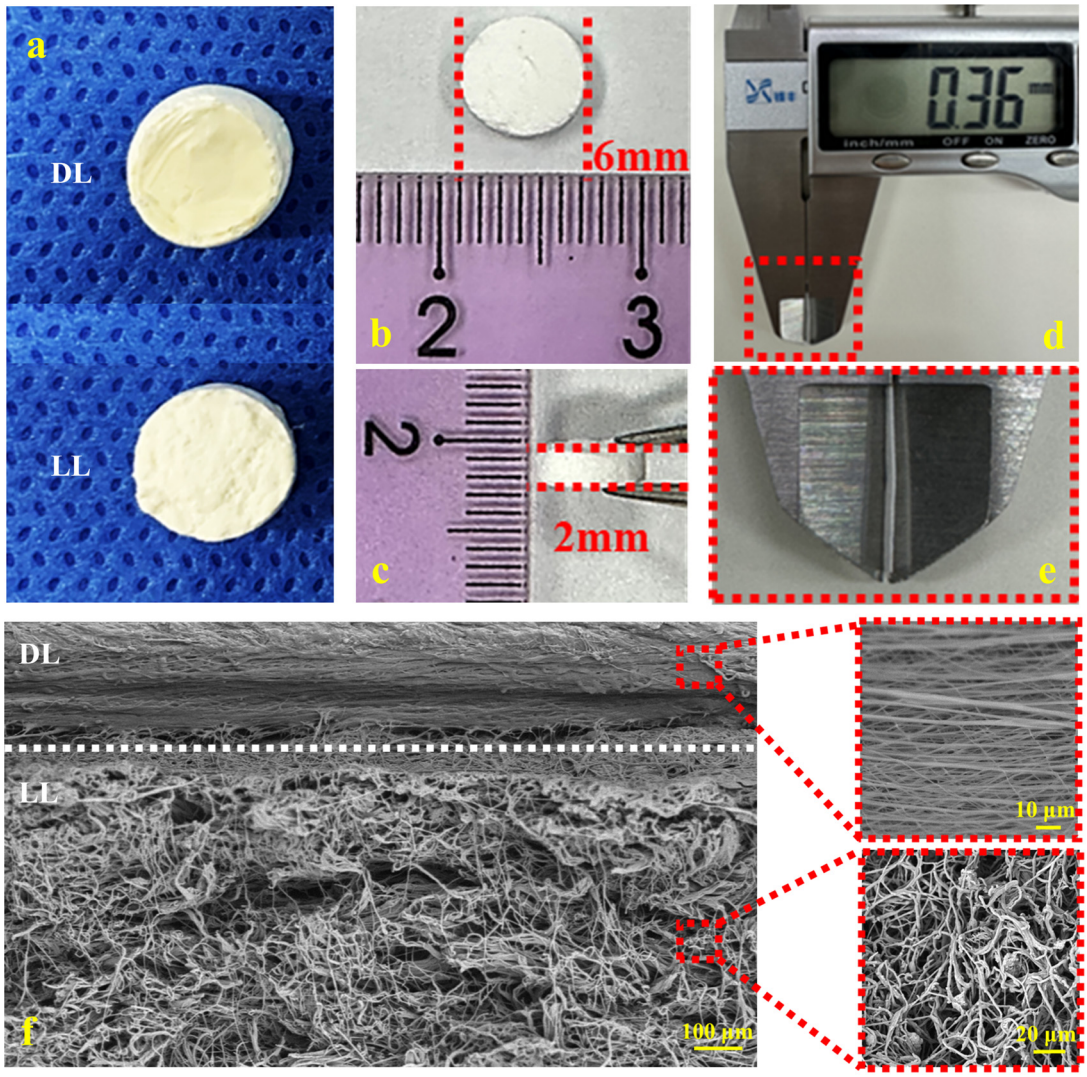

Fig. 1 Morphological characterization of the composite scaffold. (a) Photograph showing the composite scaffolds. (b and c) The width and thickness of a composite scaffold. (d and e) The thickness of the dense layer. (f) SEM images of the P/CS-T-PHA5 composite scaffold cross-section and the magnified images.

membranes. The results of CCK-8 assay suggested continuous proliferation of cells on the different aligned nanofiber membranes after culturing for 1, 3, and 5 days. However, the increase in n-HA concentration was accompanied by a gradual decrease in cell viability for M-PHA5, M-PHA7.5, and M-PHA10 (Fig. 3a). The MC3T3-E1 cells maintained an irregular shape after culturing on the different scaffolds throughout the observation period (Fig. 3b and c).

3.3. Physical characterization of the aerogels and composite scaffolds

To prepare the aerogels with a satisfactory structure, we used TBA to alter the microstructure of the freeze-dried products and facilitate the formation of loose, porous structures. The morphology of aerogels with and without TBA treatment was compared (Fig. 4a). The short fibers in the TBA-treated aerogel were evenly distributed and the structure was relatively loose. By contrast, the aerogels without TBA solvent treatment exhibit a dense structure, and the distribution of short fibers was irregular (Fig. 4a). Fig. S5a† shows the magnified SEM images of the aerogels fabricated with and without TBA treatment. The pore size of the TBA-treated aerogels was 31 ± 1 μm, 27 ± 1 μm, and 24 ± 1 μm, respectively, for the A-PHA5, A-PHA7.5, and A-PHA10 aerogels (Fig. S5b†). Due to the large pore size of the aerogels, more significant infiltration of BMSCs and promotion of their proliferation and migration were expected.[50,51] From the results, we found that the pore sizes of A-PCL, A-PHA5, A-PHA7.5, and A-PHA10 aerogels gradually decreased with the increase of n-HA concentration. This is mainly because the higher the n-HA concentration, the more complex the dispersion of n-HA in PCL solution. As such, the fibers were more likely to gather, resulting in a smaller pore size

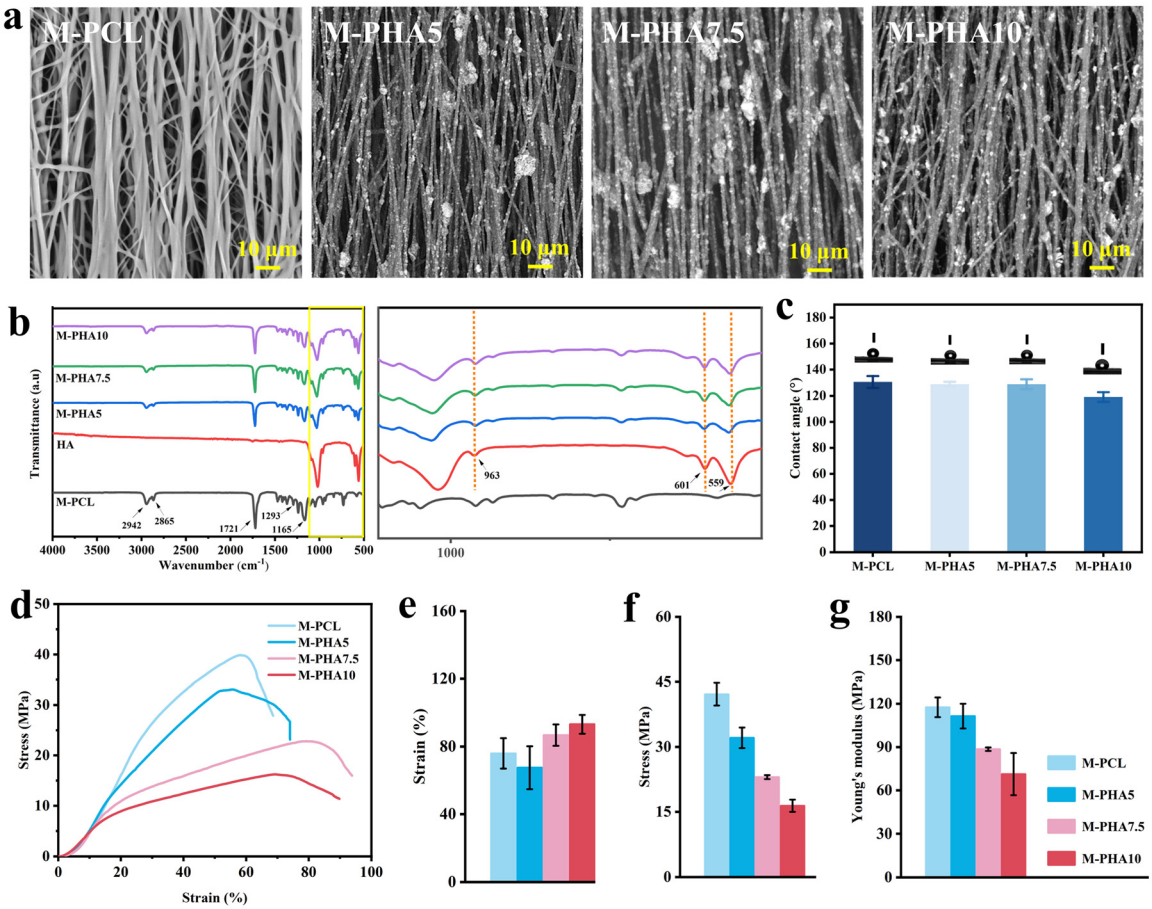

Fig. 2 Physicochemical characterization of the aligned nanofiber membranes containing different concentrations of n-HA. (a) SEM images; (b) FTIR spectra; (c) measurements of water contact angle; (d) tensile stress–strain curves; and (e–g) the ultimate strain and stress at break and Young's modulus.

during the electrospinning process.[52] As shown in Fig. S6a† FTIR spectra of the aerogels without TBA solvent treatment showed an n-HA characteristic peak. As shown in Fig. S6b† the FTIR spectra of aerogels treated with TBA indicated that using TBA during the fabrication process would not cause any changes in the characteristic peaks, confirming the preservation of n-HA in the aerogels. In Fig. S7,† the XRD patterns of n-HA and the different aerogels (A-T-PCL, A-T-PHA5, A-T-PHA7.5, and A-T-PHA10) are presented. The XRD pattern of PCL exhibited two distinct diffraction peaks at 2θ = 21.54° and 23.84°, corresponding to the (110) and (200) planes, respectively, indicating the crystallinity of PCL. The XRD pattern of n-HA revealed distinct diffraction peaks at 2θ = 25.7° (002), 31.7° (211), 39.7° (310), and 46.8° (222). No other impurities were detected, indicating the crystallinity of n-HA. The XRD pattern of the PCL/n-HA aerogel indicated that these peaks' positions remain unchanged. The results suggested the successful combination of n-HA with PCL.[53]

As illustrated in Fig. S8a,† we have prepared CS solutions with 1%, 2%, 3%, 4%, and 5% concentrations. The 1%, 2%, and 3% CS solutions were nearly completely dissolved, but the 4% and 5% CS solutions contained flocculent residues that cannot be fully dissolved. We also tested the viscosity of each CS solution (Fig. S8b†). The results indicated that the viscosity increased with the increase of the concentration. This is because the viscosity of CS aqueous solution is closely associated with its molecular structure and concentration.[54] In this study, we coated the surface of the aerogel with 3% CS solution and then received the nanofiber membrane to form a composite scaffold. Composite scaffolds were prepared using the two kinds of aerogels, and their compression properties were tested. The compressive stress–strain curves of the P/CS-T-PCL, P/CS-T-PHA5, P/CS-T-PHA7.5, and P/CS-T-PHA10 composite scaffolds are shown in Fig. 4b. The compressive stress–strain curves of their counterparts P/CS-PCL, P/CS-PHA5, P/CS-PHA7.5, and P/CS-PHA10 scaffolds are shown in Fig. S9.† The results showed that adding n-HA increases the compressive stress of the composite scaffold, and the higher the concentration of n-HA, the greater the compressive stress of the composite scaffold. A comparison of the compression modulus of the two kinds of composite scaffolds is presented in Fig. 4c. The compression moduli of the composite scaffolds

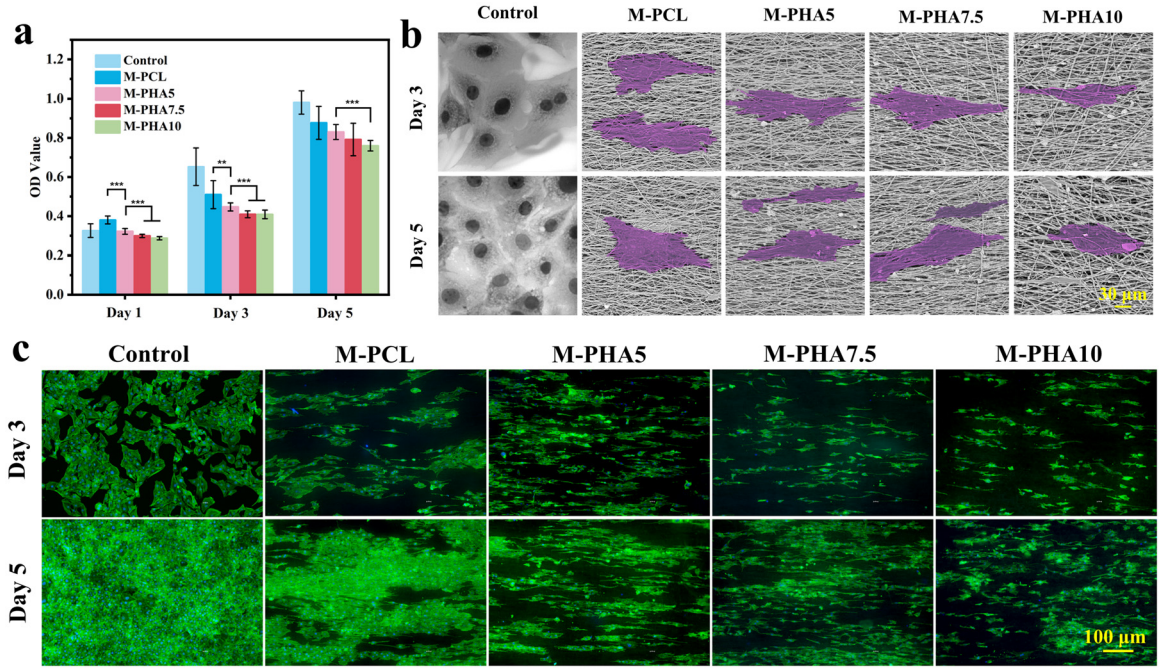

Fig. 3 (a) Cytocompatibility of the different aligned nanofiber membranes after culturing with MC3T3-E1 cells for 1, 3, and 5 days. (b) SEM and (c) fluorescence images of the morphologies of MC3T3-E1 cells after culturing on the different aligned nanofiber membranes for 3 and 5 days. Statistically significant differences are represented as ***$P < 0.001$ and **$P < 0.01$ between the compared groups.

treated with TBA were all greater than those of the untreated ones regardless of the n-HA concentrations. This can be attributed to the improved uniform pore size distribution in the TBA-treated aerogel, which contributes to a more stable structure and higher compression stress of the composite scaffolds. In addition, adding n-HA nanoparticles increased the compressive modulus of the composite scaffolds. This can be explained by the effective dispersion of n-HA in the PCL matrix and the physical crosslinking between n-HA and the PCL matrix. The n-HA nanoparticles themselves also contributed to absorbing and distributing the compressive loads.[55–57] Based on these results, it is evident that the addition of n-HA and the TBA solvent has synergistic effects on the improvement of compressive mechanical properties of the composite scaffolds.

The biodegradability of a GBR membrane is crucial for its clinical applications. It is important to allow for the coordination between scaffold degradation and tissue regeneration, as well as the structural and mechanical support during the biodegradation.[11] We investigated the degradation behavior of different composite scaffolds in PBS and artificial saliva, respectively. Artificial saliva was used to simulate the physiological environment. For GBR membranes, a suitable degradation time of 3–6 months is recommended, making it necessary to choose an appropriate scaffold for bone regeneration.[58,59] As shown in Fig. 4d and e, the P/CS-T-PCL, P/CS-T-PHA5, P/CS-T-PHA7.5, and P/CS-T-PHA10 composite scaffolds gradually degraded in 46 days in both media. The composite scaffold could provide structural support and an osteogenesis region in the early stages (around 15 days) and gradually degraded over time in artificial saliva, creating space for the regeneration of osteoblasts while maintaining partial integrity of the scaffold to promote bone regeneration. The integrity of the composite scaffolds decreased by approximately 80% in 46 days, which aligned with the bone regeneration profile (around 8 weeks), allowing for easy removal of the scaffolds and reducing secondary damage to bone tissue during scaffold removal.[12] Additionally, as shown in Fig. 4d and e, adding n-HA reduced the degradation rate of the composite scaffolds due to the difficulty in n-HA degradation in solution. With the increase of n-HA concentration, the degradation rate of the composite scaffolds was also decreased.

3.4. Evaluation of the antibacterial performance of the composite scaffolds

In clinical situations, postoperative infection is a common complication following GBR surgery. The introduction of antibacterial ingredients into composite scaffolds is beneficial for preventing infection and reducing inflammation.[60] The middle layer of the composite scaffold used in this study was a CS coating layer. The antibacterial effects of CS were evaluated using *S. aureus* and *E. coli*, respectively. As the P/CS-T-PHA5 composite scaffold exhibited notable physical properties and cell compatibility, we used the P/CS-T-PHA5 composite scaffold for further evaluation, and the P/T-PHA5 composite scaffold without the CS middle layer served as the control to investigate the antibacterial performance. The counting of

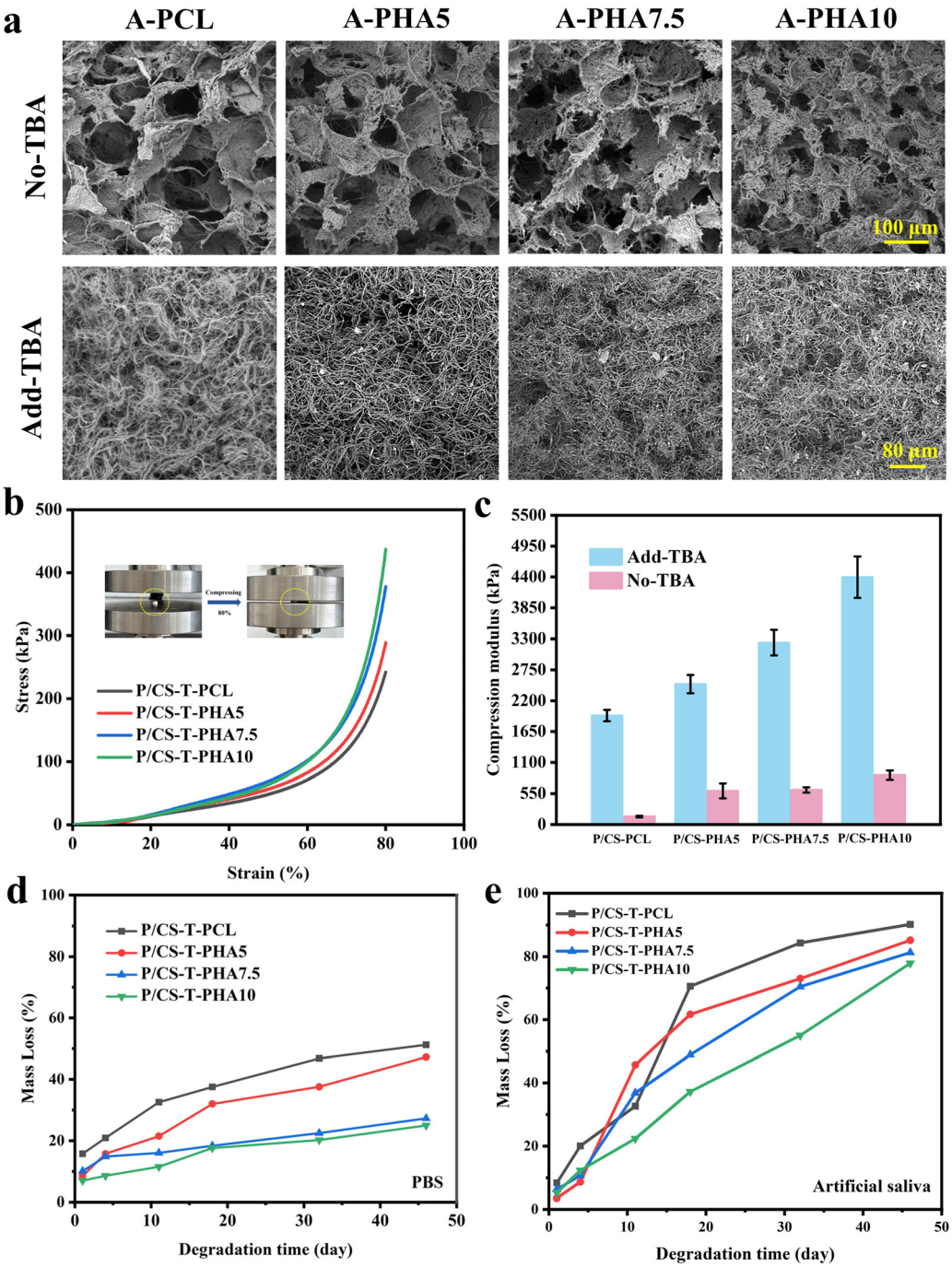

Fig. 4 (a) SEM images showing the structure of aerogels treated with or without TBA. (b) Compressive stress–strain curves of the composite scaffolds that were treated with TBA and contained different n-HA contents. (c) Compression modulus of the composite scaffolds treated with and without TBA. (d and e) Mass loss during the biodegradation of different composite scaffolds in (d) PBS and (e) artificial saliva.

colony forming units demonstrated that the colony units of *S. aureus* and *E. coli* were significantly reduced in a concentration-dependent manner after a 48-hour treatment with the P/CS-T-PHA5 scaffold. The antimicrobial rate was determined to be 98% (Fig. 5a and b). In comparison, higher bacterial colony units were observed in the control and P/T-PHA5 groups. To observe the dead or live bacteria, bacteria from different treatment groups were stained with calcein-AM (green fluorescence) and acetone iodide (red fluorescence) (Fig. 5c and d). The P/CS-T-PHA5 group effectively killed both bacteria, consistent with the previous findings. These results indicate that the composite scaffold's CS coating in the middle layer possesses significant antibacterial activity. Taken together, the middle layer can stabilize the scaffold structure

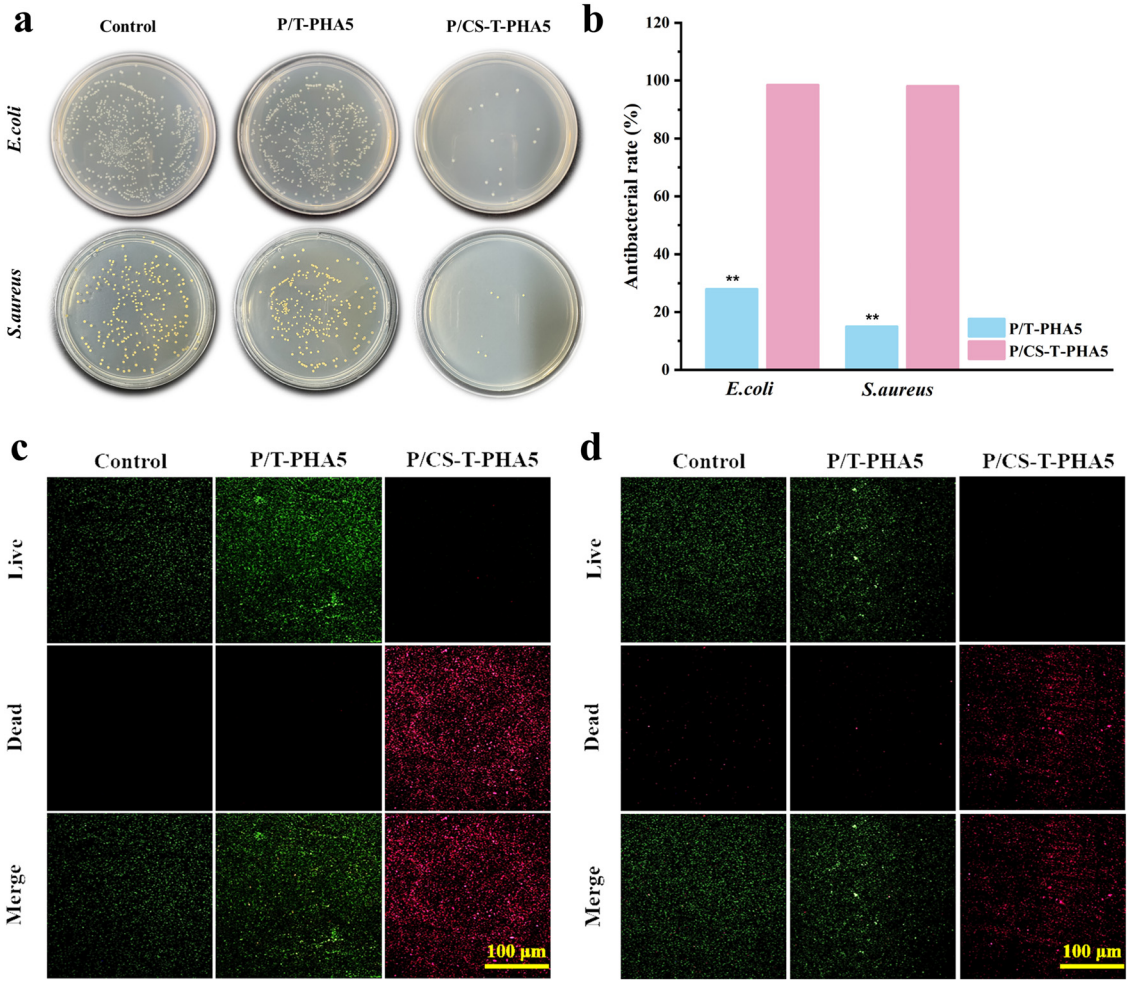

Fig. 5 (a) Photographs showing the colony distribution. (b) The antibacterial rate of the composite scaffolds with and without a CS-coating layer. $^{**}P < 0.01$ indicates the significant difference when compared with the P/CS-T-PHA5 scaffold. Fluorescence micrographs of live/dead staining of (c) *E. coli* and (d) *S. aureus* after separately cultured with the composite scaffolds.

and exhibit antibacterial properties, effectively preventing excessive inflammation during bone healing.

3.5. *In vitro* osteogenesis capability of the composite scaffolds

ALP, an osteoblast differentiation marker, was chosen to investigate the early osteogenic differentiation of BMSCs on the loose layer of the composite scaffolds. The semi-quantitative analysis of the ALP activity in Fig. 6a indicated that the ALP activity of BMSCs on the loose layer increased from day 7 to day 14 in all groups (LL-P/CS-T-PCL, LL-P/CS-T-PHA5, LL-P/CS-T-PHA7.5, LL-P/CS-T-PHA10). This finding suggests that n-HA promotes osteogenic differentiation and the formation of new bone tissues. Previous studies have shown that stem cells can absorb the dissolved phosphate ions in biomaterials to form ATP, guiding the cells to undergo osteogenic differentiation.[61] Furthermore, the role of n-HA in promoting protein adsorption and stimulating osteogenic differentiation of stem cells has been confirmed.[62] The results revealed that the expression of ALP on the loose layer of the P/CS-T-PHA5 composite scaffold was also higher than the other scaffolds.

3.6. Investigation of the barrier effect of the composite scaffolds

The P/CS-T-PHA5 composite scaffold was chosen for measuring cell infiltration due to its higher osteogenic capability. The composite scaffold's loose layer was designed to enhance cell adhesion, promote cell infiltration, and facilitate interaction between cells and the scaffold. On the other hand, the dense layer was intended to act as a physical barrier.[10] The cellular activity of NIH3T3 cells on the dense layer of the P/CS-T-PHA5 composite scaffold was also investigated (Fig. 6b). The cell proliferation on the dense layer of the scaffold (DL-P/CS-T-PCL, DL-P/CS-T-PHA5) on days 1, 3, and 5 indicated favorable cell viability.

Cell infiltration investigation was conducted to assess the infiltration depth of BMSCs in the loose layer and the barrier of NIH3T3 cells on the dense layer of the composite scaffold.

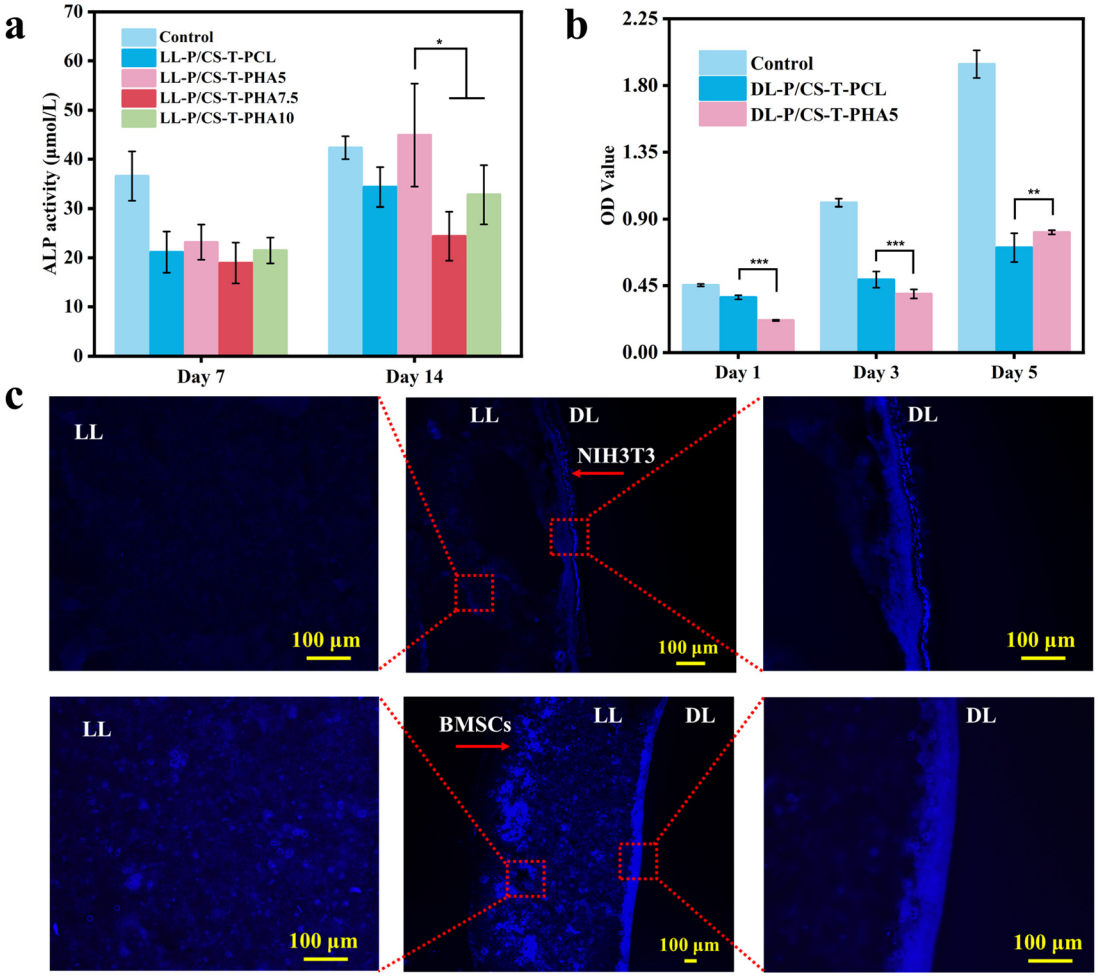

Fig. 6 (a) The ALP activity of the composite scaffolds containing different n-HA contents after culturing the BMSCs on the loose layers for 7 and 14 days. (b) Cytocompatibility of the dense layer of the composite scaffolds after culturing with the NIH3T3 fibroblasts for 1, 3, and 5 days. (c) Fluorescence micrographs showing the infiltration of BMSCs into the loose layer and the prevention of NIH3T3 fibroblasts from entering into the interior of the P/CS-T-PHA5 composite scaffold. Statistically significant differences are represented as $*P < 0.05$, $**P < 0.01$, and $***P < 0.001$ between the compared groups.

The two types of cells were co-cultured on the dense and loose layers of the P/CS-T-PHA5 composite scaffold for 7 days, and the nuclei were stained with DAPI.

The fluorescence micrographs in Fig. 6c revealed that the fibroblasts only adhered to the surface of the dense layer and did not infiltrate toward the interior of the scaffold. This is because the dense layer comprised dense and random nanofibers with small pore sizes. Thus, the dense layer could act as an excellent barrier to prevent the infiltration of fibroblasts. In comparison, the BMSCs adhered and proliferated inside the loose layer of the composite scaffold and formed extensive intercellular connections. The back of the dense layer also prevented the BMSCs from cross-growth with the fibroblasts. The specific design of this unique structure is beneficial for use in GBR, as the dense layer can block the penetration of cells in soft tissues surrounding the bone defect area. When BMSCs infiltrated the loose layer, they accelerated the process of bone regeneration. In summary, such a composite scaffold utilizes a layered structure to promote the proliferation and growth of bone cells while resisting infiltration of connective tissues, which can serve as a promising platform to guide the development of osteoblasts and promote bone repair.

Bone is an inherently porous material with a hierarchical structure. The porosity of a bone-repaired scaffold is one of the most important factors affecting its repairing performance. The appropriate porosity will increase the permeability of the scaffold and facilitate the diffusion of nutrients, promoting cell growth and activity on the scaffold. In addition, the increased surface area of the porous scaffold can also lead to better cell attachment, proliferation, and osteogenic differentiation[63,64] Geistlich Bio-Gide® and Geistlich Bio-Oss® are commonly used materials for treating clinical bone defects and guided bone tissue regeneration. They are widely utilized in combination and demonstrate favorable therapeutic outcomes. Geistlich Bio-Oss® is a bone-filling material product with an inorganic bone matrix with macroscopic and

microscopic porous structures similar to human porous bone. Geistlich Bio-Gide® is a bi-layer absorbable collagen membrane derived from porcine collagen. One layer of the membrane is porous, allowing osteoblasts to grow, while the other layer is smooth, preventing connective tissues from growing into the bone defect area. The membrane is made from natural collagen and contains no cross-linking or chemical components.[65] In this study, we developed a composite scaffold that mimics the structure of Geistlich Bio-Gide®, incorporating CS solution as the middle layer of the scaffold. CS possesses antibacterial properties, which could effectively control the bacterial environment in the bone defect area during the treatment. Overall, the composite scaffolds designed in this study can guide bone regeneration and have antibacterial and barrier properties, which have great potential for treating clinical bone defects such as skull or alveolar bone defects.

4. Conclusion

This study used PCL, n-HA, and CS as the raw materials to prepare a series of composite scaffolds for guided bone regeneration using electrospinning and freeze-drying techniques. The loose layer of the scaffold consisted of a PCL/n-HA aerogel structure, which provided a porous and supportive environment for osteoblast adhesion, infiltration, and proliferation. On the other hand, the dense layer of the scaffold was composed of a PCL random nanofiber membrane, acting as a barrier to prevent the interference of soft tissues in the bone defect area. Moreover, the middle layer of the scaffold contained a CS coating, which not only stabilized the scaffold structure but also imparted antibacterial properties, enhancing its resilience against the complex bacterial environment in the bone defect area. Among others, the P/CS-T-PHA5 composite scaffold demonstrated superior mechanical properties, coordinated degradation characteristics, antibacterial properties, and good biocompatibility. *In vitro* osteogenesis and cell infiltration evaluation also verified its good osteogenic capability. Therefore, such a specially designed composite scaffold with osteogenic, antibacterial, and barrier effects would be a promising GBR material for further related clinical applications.

Author contributions

X. D., C. Y. and X. Z. are co-first authors and completed the experiments and data analysis in the study. X. T., Q. G., M. F., and Y. W. helped with the experiments related to cell culture and antibacterial investigation and made revisions to the manuscript. Y. W., K. F. and T. W. conceived the project, funded and directed the study, and revised the manuscript. All authors approved the final manuscript.

Conflicts of interest

There are no conflicts to declare.

Acknowledgements

This work is supported by the Natural Science Foundation of Shandong Province (ZR2021YQ17), the Special Funds for Taishan Scholars Project of Shandong Province (no. tsqn202211125), the Shandong Province Key Technology R&D Program for Middle and Small Enterprises (no. 2021TSGC1189), the Young Elite Scientists Sponsorship Program by CAST (no. YESS20200097), the Shandong Province Key Technology R&D Program (nos. 2023CXGC010504, 2023CXGC010612, and 2023CXPT022), the State Key Laboratory for Biofibers and Eco-textiles (no. ZDKT202008 and ZDKT202103), the Qingdao Key Health Discipline Development Fund (2022–2024), and the Qingdao Clinical Research Center for Oral Diseases (22-3-7-lczx-7-nsh). The authors also thank the "Advanced Biomaterials and Regenerative Medicine (ABRM)" Innovation Team supported by the Young-Talent Introduction and Cultivation Plan in the Universities of Shandong Province.

References

1 P. Aprile, D. Letourneur and T. Simon-Yarza, *Adv. Healthcare Mater.*, 2020, **9**, 2000707.
2 K. Kim, Y. Su, A. J. Kucine, K. Cheng and D. Zhu, *ACS Biomater. Sci. Eng.*, 2023, **9**, 5457–5478.
3 X. Liu, W. Chen, B. Shao, X. Zhang, Y. Wang, S. Zhang and W. Wu, *Biomaterials*, 2021, **276**, 120998.
4 Q. Wang, X. Ran, J. Wang, S. Wang, P. Zhang, E. Gao, B. Bai, J. Zhang, G. Zhou and D. Lei, *Adv. Fiber Mater.*, 2023, **5**, 1008–1024.
5 Y. Wang, Y. Liu, X. Zhang, N. Liu, X. Yu, M. Gao, W. Wang and T. Wu, *Front. Chem.*, 2021, **9**, 797523.
6 Y. Bian, T. Hu, Z. Lv, Y. Xu, Y. Wang, H. Wang, W. Zhu, B. Feng, R. Liang, C. Tan and X. Weng, *Exploration*, 2023, **3**, 20210105.
7 Y. Ren, L. Fan, S. Alkildani, L. Liu, S. Emmert, S. Najman, D. Rimashevskiy, R. Schnettler, O. Jung, X. Xiong and M. Barbeck, *Int. J. Mol. Sci.*, 2022, **23**, 14987.
8 Z. Chen, L. Chen, R. Liu, Y. Liu, S. Chen, S. Lu, Z. Lin, Z. Chen, C. Wu and Y. Xiao, *Biomater. Sci.*, 2018, **6**, 1007–1019.
9 S. Abtahi, X. Chen, S. Shahabi and N. Nasiri, *ACS Mater. Au*, 2023, **3**, 394–417.
10 F. C. Menezes, N. M. Siqueira, S. Fung, J. M. Scheibel, D. J. Moura, M. Guvendiren, J. Kohn and R. M. D. Soares, *Polym. Adv. Technol.*, 2022, **33**, 2682–2695.
11 M. Lian, Y. Han, B. Sun, L. Xu, X. Wang, B. Ni, W. Jiang, Z. Qiao, K. Dai and X. Zhang, *Acta Biomater.*, 2020, **118**, 83–99.

12 Q. Wang, Y. Feng, M. He, W. Zhao, L. Qiu and C. Zhao, *Adv. Funct. Mater.*, 2021, **31**, 2008906.
13 X. Shen, Z. Zhang, C. Cheng, C. Liu, N. Ma, D. Sun, D. Li and C. Wang, *Biomed. Technol.*, 2024, **5**, 87–101.
14 J. Mu, D. Luo, W. Li and Y. Ding, *Biomed. Technol.*, 2024, **5**, 60–72.
15 C. Yu, T. Wang, H. Diao, N. Liu, Y. Zhang, H. Jiang, P. Zhao, Z. Shan, Z. Sun, T. Wu, X. Mo and T. Yu, *Adv. Fiber Mater.*, 2022, **4**, 908–922.
16 G. Mizraji, A. Davidzohn, M. Gursoy, U. K. Gursoy, L. Shapira and A. Wilensky, *Periodontol. 2000*, 2023, **93**, 56–76.
17 K. Chen, L. Zhao, J. Sun, X. Gu, C. Huang, H. Su and Y. Fan, *Sci. China Mater.*, 2022, **65**, 2627–2646.
18 Y. Liu, X. Zhang, Y. Wang, M. Guo, J. Sheng, Y. Wang and T. Wu, *Chem. Commun.*, 2023, **59**, 10753–10756.
19 S. Wei, J. Ma, L. Xu, X. Gu and X. Ma, *Mil. Med. Res.*, 2020, **7**, 1–25.
20 S. Liu, J. Yu, Y. Gan, X. Qiu, Z. Gao, H. Wang, S. Chen, Y. Xiong, G. Liu, S. Lin, A. McCarthy, J. John, D. Wei and H. Hou, *Mil. Med. Res.*, 2023, **10**, 16.
21 Y. Tian, D. Wu, D. Wu, Y. Cui, G. Ren, Y. Wang, J. Wang and C. Peng, *Front. Bioeng. Biotechnol.*, 2022, **10**, 899760.
22 C. Ardean, C. M. Davidescu, N. S. Nemeș, A. Negrea, M. Ciopec, N. Duteanu, P. Negrea, D. Duda-Seiman and V. Musta, *Int. J. Mol. Sci.*, 2021, **22**, 7449.
23 Y. Yang, M. Li, B. Zhou, X. Jiang, D. Zhang, H. Luo and S. Lei, *Adv. Ther.*, 2022, **5**, 2200043.
24 I. Elgali, O. Omar, C. Dahlin and P. Thomsen, *Eur. J. Oral Sci.*, 2017, **125**, 315–337.
25 X. Ding, J. Ma, T. Fan, R. Issa, Y. Li, D. Weng, D. Zhang and Y. Chen, *Interdiscip. Med.*, 2024, **2**, e20230045.
26 E. Sadeghi, S. M. Zebarjad, F. Khademi and E. Bagherzadeh, *Polym. Compos.*, 2022, **43**, 7379–7389.
27 A. Rezaei and M. R. Mohammadi, *Mater. Sci. Eng., C*, 2013, **33**, 390–396.
28 P. Wu, L. Shen, H. Liu, X. Zou, J. Zhao, Y. Huang, Y. Zhu, Z. Li, C. Xu, L. Luo, Z. Luo, M. Wu, L. Cai, X. Li and Z. Wang, *Mil. Med. Res.*, 2023, **10**, 35.
29 J. Xue, T. Wu, Y. Dai and Y. Xia, *Chem. Rev.*, 2019, **119**, 5298–5415.
30 R. K. Mishra, P. Mishra, K. Verma, A. Mondal, R. G. Chaudhary, M. M. Abolhasani and S. Loganathan, *Environ. Chem. Lett.*, 2019, **17**, 767–800.
31 Y. Liu, Q. Guo, X. Zhang, Y. Wang, X. Mo and T. Wu, *Adv. Fiber Mater.*, 2023, **5**, 1241–1272.
32 Y. Zhang, M. Zhang, D. Cheng, S. Xu, C. Du, L. Xie and W. Zhao, *Biomater. Sci.*, 2022, **10**, 1423–1447.
33 J. Hashemi, G. Barati, S. E. Enderami and M. Safdari, *Mater. Today Commun.*, 2020, **25**, 101561.
34 H. P. Dang, C. Vaquette, T. Shabab, R. A. Pérez, Y. Yang, T. R. Dargaville, A. Shafiee and P. A. Tran, *Appl. Mater. Today*, 2020, **20**, 100706.
35 T. Weigel, C. Malkmus, V. Weigel, M. Wußmann, C. Berger, J. Brennecke, F. Groeber-Becker and J. Hansmann, *Adv. Mater.*, 2022, **34**, 2106780.
36 D. Karanth, K. Song, M. L. Martin, D. R. Meyer, C. Dolce, Y. Huang and L. S. Holliday, *Macromol. Biosci.*, 2022, **22**, 2100441.
37 D. Zong, X. Zhang, X. Yin, F. Wang, J. Yu, S. Zhang and B. Ding, *Adv. Fiber Mater.*, 2022, **4**, 1434–1462.
38 Y. Tan, D. Chen, Y. Wang, W. Wang, L. Xu, R. Liu, C. You, G. Li, H. Zhou and D. Li, *Macromol. Biosci.*, 2022, **22**, 2100441.
39 Z. Mao, J. Bai, X. Jin, W. Mao and Y. Dong, *Colloids Surf., B*, 2021, **208**, 112070.
40 Y. Pan, J. Zheng, Y. Xu, X. Chen, M. Yan, J. Li, X. Zhao, Y. Feng, Y. Ma, M. Ding, R. Wang and J. He, *J. Colloid Interface Sci.*, 2022, **628**, 829–839.
41 N. Rai and I. Chauhan, *J. Sol-Gel Sci. Technol.*, 2023, **105**, 324–336.
42 N. Liu, X. Zhang, Q. Guo, T. Wu and Y. Wang, *Front. Mater.*, 2022, **9**, 925321.
43 Z. Kuang, G. Dai, R. Wan, D. Zhang, C. Zhao, C. Chen, J. Li, H. Gu and W. Huang, *Genes Dis.*, 2021, **8**, 193–202.
44 H. Yao, J. Wang, Y. Deng, Z. Li and J. Wei, *Int. J. Biol. Macromol.*, 2023, **247**, 125671.
45 H. Sun, C. Zhang, B. Zhang, P. Song, X. Xu, X. Gui, X. Chen, G. Lu, X. Li, J. Liang, J. Sun, Q. Jiang, C. Zhou, Y. Fan, X. Zhou and X. Zhang, *Chem. Eng. J.*, 2022, **427**, 130961.
46 J. Wu, R. Fu, M. Xiao, Q. Zheng, L. Wu, K. Fang and Y. Ren, *Chem. Eng. J.*, 2024, **481**, 148453.
47 J. Meng, G. Yang, L. Liu, Y. Song, L. Jiang and S. Wang, *Sci. China: Chem.*, 2017, **60**, 614–620.
48 S. Li, T. Wang, J. Hu, B. Wang, Y. Li, L. Wang, G. Li, J. Zhang and Z. Zhou, *Polym. Compos.*, 2021, **42**, 6512–6522.
49 S. Jin, F. Sun, Q. Zou, J. Huang, Y. Zuo, Y. Li, S. Wang, L. Cheng, Y. Man, F. Yang and J. Li, *Biomacromolecules*, 2019, **20**, 2058–2067.
50 N. Alsenany, S. F. Mansour and S. S. Eldera, *New J. Chem.*, 2022, **46**, 14816–14825.
51 J. Xie, H. Shen, G. Yuan, K. Lin and J. Su, *Mater. Sci. Eng., C*, 2021, **120**, 111787.
52 D. Xia, Y. Wang, R. Wu, Q. Zheng, G. Zhang, S. Xu and P. Zhou, *Appl. Mater. Today*, 2022, **29**, 101607.
53 S. Solechan, A. Suprihanto, S. A. Widyanto, J. Triyono, D. F. Fitriyana, J. P. Siregar and T. Cionita, *Polymers*, 2023, **15**, 559.
54 I. Kondratowicz, I. Shalayel, M. Nadolska, S. Tsujimura, Y. Yamagata, I. Shitanda and A. Zebda, *J. Polym. Environ.*, 2023, **31**, 1221–1231.
55 M. Rajabi, J. D. Cabral, S. Saunderson, M. Gould and M. A. Ali, *Biomed. Mater.*, 2023, **18**, 065009.
56 J. A. Killion, L. M. Geever, D. M. Devine, H. Farrell and C. L. Higginbotham, *Int. J. Polym. Mater. Polym. Biomater.*, 2014, **63**, 641–650.
57 J. Corona-Gomez, X. Chen and Q. Yang, *J. Funct. Biomater.*, 2016, **7**, 18.
58 C. Liu, J. Wu, D. Gan, Z. Li, J. Shen, P. Tang, S. Luo, P. Li, X. Lu and W. Zheng, *J. Biomed. Mater. Res., Part B*, 2020, **108**, 1814–1825.
59 M. Koolen, S. Yavari, K. Lietaert, R. Wauthle, A. Zadpoor and H. Weinans, *Materials*, 2020, **13**, 1992.

60 M. Lian, B. Sun, Z. Qiao, K. Zhao, X. Zhou, Q. Zhang, D. Zou, C. He and X. Zhang, *Colloids Surf., B*, 2019, **176**, 219–229.
61 H. Kang, Y. Shih, M. Nakasaki, H. Kabra and S. Varghese, *Sci. Adv.*, 2016, **2**, e1600691.
62 C. Zhao, X. Wang, L. Gao, L. Jing, Q. Zhou and J. Chang, *Acta Biomater.*, 2018, **73**, 509–521.
63 D. Jeyachandran and M. Cerruti, *Adv. Eng. Mater.*, 2023, **25**, 2201743.
64 Y. Wang, Q. Guo, W. Wang, Y. Wang, K. Fang, Q. Wan, H. Li and T. Wu, *Nanoscale*, 2022, **14**, 18217–18230.
65 S. R. V. da Silva, R. M. Pagnoncelli, J. V. Paes, R. Aquino, M. Warmeling and R. Valiati, *J. Dent. Health Oral Disord. Ther.*, 2018, **9**, 181–182.